



$\text{Cd}_{0.2}\text{Zn}_{0.8}\text{S@UiO-66-NH}_2$ nanocomposites as efficient and stable visible-light-driven photocatalyst for H_2 evolution and CO_2 reduction

Yun Su, Zhe Zhang, Hong Liu*, Yong Wang*

Department of Chemical Engineering, School of Environmental and Chemical Engineering, Shanghai University, 99 Shangda Road, Shanghai 200444, PR China

ARTICLE INFO

Article history:

Received 19 April 2016

Received in revised form 5 July 2016

Accepted 19 July 2016

Available online 19 July 2016

Keywords:

Metal-organic frameworks

Photocatalysis

H_2 evolution

CO_2 reduction

$\text{Cd}_x\text{Zn}_{1-x}\text{S}$

ABSTRACT

Metal-organic frameworks (MOFs), a new class of porous crystalline materials, have attracted great interest as fascinating materials for sustainable energy and environmental remediation. However, the functionalization and diversification of MOFs are still challenging and imperative for the development of highly active MOF-based materials. In this study, a series of $\text{Cd}_{0.2}\text{Zn}_{0.8}\text{S@UiO-66-NH}_2$ nanocomposites with different UiO-66-NH₂ contents were fabricated via a facile solvothermal method. The photocatalytic performances of the obtained $\text{Cd}_{0.2}\text{Zn}_{0.8}\text{S@UiO-66-NH}_2$ nanocomposites were evaluated by photocatalytic H_2 evolution and CO_2 reduction under visible-light irradiation. The resultant hybrids exhibit significantly enhanced photocatalytic activity for hydrogen evolution and CO_2 reduction as compared with pristine components, and the optimal UiO-66-NH₂ content is 20 wt%. The composite can show a hydrogen evolution rate of 5846.5 $\mu\text{mol h}^{-1} \text{g}^{-1}$ and a CH_3OH production rate of 6.8 $\mu\text{mol h}^{-1} \text{g}^{-1}$. The remarkable enhancement of the photocatalytic activity should be attributed to the efficient charge separation and transfer on the interface between $\text{Cd}_{0.2}\text{Zn}_{0.8}\text{S}$ and UiO-66-NH₂. Furthermore, the $\text{Cd}_{0.2}\text{Zn}_{0.8}\text{S@UiO-66-NH}_2$ photocatalysts show excellent stability during photocatalytic hydrogen evolution and CO_2 reduction. This work demonstrates that MOF-based composite materials hold great promise for applications in the field of energy conversion and environmental purification.

© 2016 Elsevier B.V. All rights reserved.

1. Introduction

In the past few decades, semiconductor-based photocatalysis has attracted great attention because of its potential for solving energy and environmental problems [1–5]. Among the various photocatalytic reactions, the splitting of H_2O to H_2 and the reduction of CO_2 to chemical fuels are two of the most important and challenging reactions. To date, various kinds of photocatalysts, such as TiO_2 [6], BiVO_4 [7], Bi_2WO_6 [8], Zn_2GeO_4 [9], $\text{Zn}_2\text{Ga}_2\text{O}_4$ [10], NaNbO_3 [11], CdS [12], etc, have been explored for applications in these two reactions. However, the quantum yield and solar energy conversion efficiency of these developed photocatalysts are still relatively low, which limits their practical applications. Therefore, it is still attractive to explore new photocatalysts with low cost, improved activities and high stability.

As the solid solution of CdS and ZnS , $\text{Cd}_x\text{Zn}_{1-x}\text{S}$ possesses a tunable composition as well as a band gap. The newly formed energy band in $\text{Cd}_x\text{Zn}_{1-x}\text{S}$ could respond to visible light. Previous studies have revealed that $\text{Cd}_x\text{Zn}_{1-x}\text{S}$ is active for water splitting H_2 -production and degradation of organic pollutants under visible light irradiation and shows a considerable chemical stability [13–15]. However, the photocatalytic activity of pristine $\text{Cd}_x\text{Zn}_{1-x}\text{S}$ is low because of the poor separation efficiency and low migration ability of the photoexcited charge carriers [1]. Some efforts have been performed to enhance the photocatalytic performance of $\text{Cd}_x\text{Zn}_{1-x}\text{S}$. For example, by controlling morphologies of $\text{Cd}_x\text{Zn}_{1-x}\text{S}$ [16], doping with noble metals [17], and incorporation of reduced graphene oxide [1,18] or other semiconductors [19], the photocatalytic performance of $\text{Cd}_x\text{Zn}_{1-x}\text{S}$ has been enhanced to a certain degree. Unfortunately, the photocatalytic activity of the $\text{Cd}_x\text{Zn}_{1-x}\text{S}$ photocatalyst is still far from the fundamental requirement of practical application. Thus development of novel approaches for the modification of the $\text{Cd}_x\text{Zn}_{1-x}\text{S}$ photocatalyst is highly desired. Additionally, to the best of our knowledge, there is no report about the $\text{Cd}_x\text{Zn}_{1-x}\text{S}$ -based material used as photocatalyst for CO_2 reduction so far.

* Corresponding authors.

E-mail addresses: liuhong@shu.edu.cn (H. Liu), yongwang@shu.edu.cn (Y. Wang).

Metal-organic frameworks (MOFs) are a fascinating class of porous crystalline materials built from metal ions and polyfunctional organic ligands. They have attracted significant research interest in recent years mainly due to their tunable pore sizes, high specific surface areas, the possibility to functionalize, and designable framework structures [20–22]. Taking advantage of these features, MOFs have been widely studied for many applications such as gas storage [23], gas separation [24], heterogeneous catalysis [21,25], nonlinear optics [26], biomedical imaging [27], chemical sensing [28] and drug delivery [22,29]. In addition, recent researches demonstrate some MOFs exhibit semiconductor behavior and can be used as photocatalyst. In fact, more and more photocatalysts based on MOFs applied in the degradation of organic pollutants (e.g. MOF-5, UTSA-38, MIL-100(Fe), MIL-53(Fe), MIL-88A and ZIF-8), hydrogen evolution (UiO-66), CO₂ reduction (e.g. UiO-67, MOF-253, MIL-53(Fe), NH₂-MIL-125(Ti) and NH₂-UiO-66), and organic transformations (e.g. UiO-67, MIL-100(Fe), NH₂-MIL-125(Ti) and NH₂-MIL-101(Fe)) have already been reported [30–45]. Compared with traditional semiconductor photocatalysts, the MOF photocatalysts are beneficial because various combinations of metal-oxo clusters and bridging organic linkers allow for fine-tuning and rational design of these photocatalysts at the molecular level. Furthermore, intrinsic porosity of MOFs facilitates the diffusion of substrates and products through the open framework structures [46,47]. Despite the rapidly growing interest in MOFs, the studies on MOF-based photocatalysis are still in the infancy stage and the photocatalytic performances of MOFs have yet to be fully exploited. The previous MOFs-derived photocatalysts are still subject to some drawbacks such as low quantum efficiency and poor stability. To enhance the photocatalytic performance of MOFs, some strategies such as metal [48] or ligand substitution [44] and noble metal deposition [49] have been employed. Besides, the formation of heterostructure by coupling MOFs with light-harvesting semiconductor materials is also a feasible route to promote the separation of photogenerated charge carriers and thus increase the photocatalytic activity. Recently, semiconductor@MOF heterostructures like ZnO@ZIF-8 [50], Cu₃(BTC)₂@TiO₂ [51], BiVO₄@MIL-101 [52], Bi₂WO₆@UiO-66 [53], BiOBr@UiO-66 [54], UiO-66@g-C₃N₄ [55], CdS@UiO-66-NH₂ [47] and MoS₂@UiO-66@CdS [46] have been synthesized and show great advantages due to their synergistic effect. Nevertheless, up to now studies concerning MOF-based hybrid photocatalysts are still scarce. In particular, the photocatalytic activities of Cd_xZn_{1-x}S@MOF nanocomposites, to the best of our knowledge, have not been investigated.

In this work, we report for the first time a new hybrid photocatalyst made by coupling amino-functionalised Zr-based MOF (UiO-66-NH₂) and Cd_xZn_{1-x}S. UiO-66-NH₂ was chosen as the metal-organic framework material owing to its large surface area, excellent thermal and chemical stability, visible-light responsiveness and semiconductor property [46,47,53–56]. Our preliminary experiments showed that, among pristine Cd_xZn_{1-x}S solid solutions with different stoichiometries, the Cd_{0.2}Zn_{0.8}S solid solution exhibited the highest photocatalytic activity for H₂-production and CO₂ reduction. Therefore, Cd_{0.2}Zn_{0.8}S solid solution was used in this study. Here, we developed a facile solvothermal method to prepare a series of UiO-66-NH₂ supported Cd_{0.2}Zn_{0.8}S nanocomposites with different UiO-66-NH₂ contents. The obtained Zn_{0.8}Cd_{0.2}S@UiO-66-NH₂ nanocomposites showed excellent high photocatalytic activity and stability in H₂-production and CO₂ reduction under visible light ($\lambda > 420$ nm) irradiation. Furthermore, the possible mechanism for the excellent photocatalytic performance of Zn_{0.8}Cd_{0.2}S@UiO-66-NH₂ is also proposed. We hope that the current work could inspire growing interest on the fabrication of other high-performance semiconductor@MOFs composite by taking the advantage of MOFs.

2. Experimental

2.1. Materials

Zirconium tetrachloride (ZrCl₄), *N,N*-dimethyl formamide (DMF), cadmium acetate dihydrate (Cd(CH₃COO)₂·2H₂O), zinc acetate dihydrate (Zn(CH₃COO)₂·2H₂O), sodium sulfide nonahydrate (Na₂S·9H₂O), methanol and ethylene glycol (EG) were purchased from Sinopharm Chemical Reagent Co., Ltd. 2-Aminoterephthalic acid (ATA) was obtained from Tokyo Chemical Industry Co., Ltd. All the reagents were of analytical grade and were used without further purification.

2.2. Synthesis

2.2.1. Synthesis of UiO-66-NH₂

UiO-66-NH₂ was synthesized using the same procedure reported previously [47]. In a typical synthesis, 0.2332 g ZrCl₄ and 0.1812 g ATA were dissolved in 50 mL DMF, and then the mixture solution was transferred to a 100 mL Telton-lined stainless steel autoclave. The autoclave was sealed and heated in an electrical oven at 120 °C for 48 h under autogenous pressure. After cooling naturally, the obtained sample was centrifuged and washed with anhydrous methanol for several times to remove the residual DMF. The final product was dried under vacuum at 100 °C for 12 h.

2.2.2. Synthesis of Cd_{0.2}Zn_{0.8}S@UiO-66-NH₂

The Cd_{0.2}Zn_{0.8}S@UiO-66-NH₂ composites were obtained by a one-step solvothermal method. In detail, 0.133 g Cd(AC)₂·2H₂O and 0.439 g Zn(AC)₂·2H₂O were dissolved in 30 mL EG to form a homogeneous solution. Meanwhile, an appropriate amount of as-prepared UiO-66-NH₂ sample was dispersed in 10 mL EG by sonication for 0.5 h. The obtained UiO-66-NH₂ solution was added to the above mixed salt solution gradually and stirred for 1 h at room temperature. After that, 10 mL 0.3 M Na₂S aqueous solution was added dropwise with continuous stirring. After being stirred for 2 h, the suspension was transferred to a 100 mL Teflon-lined autoclave and maintained at 160 °C for 4 h. The final product was collected by centrifugation, washing with ethanol and deionized water, and drying in an oven at 80 °C for 24 h. The as-synthesized Cd_{0.2}Zn_{0.8}S@UiO-66-NH₂ samples with 10 wt%, 20 wt%, 30 wt% and 40 wt% UiO-66-NH₂ were labeled as CZS@UN10, CZS@UN20, CZS@UN30 and CZS@UN40 respectively. For comparison, the pure Cd_{0.2}Zn_{0.8}S sample was also prepared using the same solvothermal method in the absence of UiO-66-NH₂.

2.3. Characterization

The crystal structure of the as-prepared samples was identified by an X-ray diffractometer (XRD, D/MAX-2550) using Cu K α radiation. The morphologies and microstructures of the samples were analyzed by the transmission electron microscope (TEM, JEOL 200CX) with an energy-dispersive X-ray (EDX) spectrometer and high-resolution transmission electron microscope (HRTEM, JEM-2010F). The X-ray photoelectron spectroscopy (XPS) measurement was carried out in PHI ESCA-5000C electron spectrometer. N₂ adsorption-desorption isotherms were obtained at -196 °C on a Micromeritics ASAP 2460 Sorptometer using static adsorption procedures, and the Brunauer-Emmett-Teller (BET) surface areas and pore size distributions were calculated by using N₂ adsorption-desorption isotherms. UV-vis absorption spectra of the samples were recorded on a UV-vis spectrophotometer (Hitachi U-3010) with a wavelength range of 200–800 nm. Photoluminescence (PL) spectra were measured using a Hitachi F-7000 fluorescence spectrophotometer at room temperature. Thermo-gravimetric analysis (TGA) was performed on a TA Q50 thermal analyzer under nitrogen

atmosphere with a heating rate of $10^{\circ}\text{C min}^{-1}$. The concentration of the Cd and Zn ions in solution was quantified by an inductively coupled plasma emission spectroscopy (ICP, PERKINE 7300DV).

2.4. Photocatalytic test

The photocatalytic hydrogen evolution experiments were performed at room temperature in a 100 mL quartz reactor, which is connected with a closed-cycle circulation system. The visible light was provided by a 300 W Xenon lamp (PLS-SXE300C, Beijing Perfectlight Co. Ltd., China) coupled with a UV cut-off filter ($\lambda > 420$ nm). In a typical experiment, 0.05 g of photocatalyst powder was dispersed in 100 mL of aqueous solution containing 0.1 M Na_2S and 0.1 M Na_2SO_3 . The reaction vessel was evacuated by N_2 for 30 min to remove dissolved oxygen before photocatalytic experiments. The reaction cell was kept at room temperature with cooling water. The produced H_2 was detected using an online gas chromatography (GC7900, N_2 carrier, 5A molecular sieve column, TCD detector).

The photocatalytic reduction of CO_2 experiment was conducted in a closed gas circulation system equipped with a 300 W Xe lamp combined with a 420 nm cut-off filter as a light source. All experiments were performed at room temperature. In each run, 0.1 g photocatalyst was dispersed in 100 mL aqueous solution containing 0.1 M NaOH. To prevent the reactor being interfered with outside light, the system was covered by tinfoil. Before irradiation, CO_2 (99.995%) was bubbled through the reactor for 30 min to eliminate dissolved oxygen and saturate the solution. Then, the suspension was exposed to visible light irradiation under magnetic stirring. At given time intervals, about 1 mL suspensions were collected and centrifuged to remove the photocatalyst particles. The concentrations of reduction product were analyzed using a GC7900 gas chromatography equipped with a FID detector and a capillary column (TM-PLOT U, 30 m \times 0.53 mm \times 20 μm).

2.5. Photocurrent measurements

Photocurrent measurements were performed on a CHI-660 electrochemical workstation (Chenhua Instrument, Shanghai, China) in a conventional three electrode configuration with a Pt foil as the counter electrode and an Ag/AgCl (saturated KCl) as the reference electrode. A 300 W Xe arc lamp served as a light source. A 0.5 M Na_2SO_4 aqueous solution was used as the electrolyte. The working electrodes were prepared as follows: 10 mg of the prepared photocatalyst was ground with 20 μL of a poly (3, 4-ethylenedioxythiophene)/poly(styrenesulfonate) (PEDOT/TPSS, 1.3–1.7%) aqueous solution and 100 μL of distilled water to make a slurry. The slurry was then spread on a 1.5 cm \times 1.0 cm indium-tin oxide (ITO) glass substrate with an active area of about 0.3 cm^2 by the doctor-blade method, using adhesive tape as the space. Finally, the electrode was dried in an oven and annealed at 150 $^{\circ}\text{C}$ for 30 min.

3. Results and discussion

3.1. $\text{Cd}_x\text{Zn}_{1-x}\text{S}$ solid solutions

Fig. S1 shows the XRD patterns of $\text{Cd}_x\text{Zn}_{1-x}\text{S}$ samples synthesized by a solvothermal method. The XRD patterns for $x = 0.0$ and 1.0 are identical to those reported for ZnS [JCPDS No. 05-0566] and CdS [JCPDS No. 10-0454], respectively. With increasing x , the diffraction peaks shift to smaller-angle side. The gradual shift of the XRD pattern as a function of x indicates that the samples are not mixtures of ZnS and CdS phases but $\text{Cd}_x\text{Zn}_{1-x}\text{S}$ solid solutions.

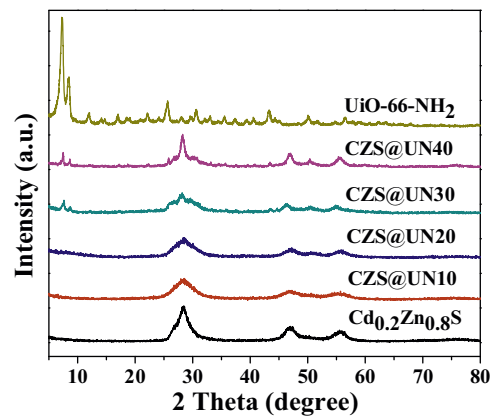


Fig. 1. XRD patterns of pure UiO-66-NH_2 , $\text{Cd}_{0.2}\text{Zn}_{0.8}\text{S}$ and $\text{Cd}_{0.2}\text{Zn}_{0.8}\text{S@UiO-66-NH}_2$ composites.

It is well-known that the photocatalytic activity of $\text{Cd}_x\text{Zn}_{1-x}\text{S}$ can be altered by varying the Cd/Zn ratio. Fig. S2 shows that the prepared $\text{Cd}_x\text{Zn}_{1-x}\text{S}$ solid solution without UiO-66-NH_2 exhibits the highest photocatalytic activity for H_2 -production and CO_2 reduction at $x = 0.2$, thus $\text{Cd}_{0.2}\text{Zn}_{0.8}\text{S}$ solid solution was used in the following study.

3.2. $\text{Cd}_{0.2}\text{Zn}_{0.8}\text{S@UiO-66-NH}_2$ composites

3.2.1. Materials characterization

Thermo-gravimetric analysis was performed from room temperature to 800 $^{\circ}\text{C}$ under nitrogen conditions to determine the real content of UiO-66-NH_2 in the $\text{Cd}_{0.2}\text{Zn}_{0.8}\text{S@UiO-66-NH}_2$ nanocomposites and the results are shown in Fig. S3. From which the residual quantity can be obtained for UiO-66-NH_2 , $\text{Cd}_{0.2}\text{Zn}_{0.8}\text{S}$ and $\text{Cd}_{0.2}\text{Zn}_{0.8}\text{S@UiO-66-NH}_2$ composites. Then the $\text{Cd}_{0.2}\text{Zn}_{0.8}\text{S}$ to UiO-66-NH_2 mass ratio ($\frac{m_{\text{CZS}}}{m_{\text{UN}}}$) in composites can be calculated by the following equation [52]:

$$\frac{m_{\text{CZS}}}{m_{\text{UN}}} = \frac{r_{\text{CZSCN}} - r_{\text{UN}}}{r_{\text{CZS}} - r_{\text{CZSCN}}},$$

where r_{CZSCN} , r_{CZS} and r_{UN} are the residual mass fraction (%) of $\text{Cd}_{0.2}\text{Zn}_{0.8}\text{S@UiO-66-NH}_2$, $\text{Cd}_{0.2}\text{Zn}_{0.8}\text{S}$ and UiO-66-NH_2 , respectively. As shown in Table S1, the real UiO-66-NH_2 contents are nearly consistent with the theoretical values.

Fig. 1 shows the XRD patterns of pure $\text{Cd}_{0.2}\text{Zn}_{0.8}\text{S}$, UiO-66-NH_2 , and $\text{Cd}_{0.2}\text{Zn}_{0.8}\text{S@UiO-66-NH}_2$ nanocomposites with different weight contents of UiO-66-NH_2 . The XRD pattern of as-synthesized UiO-66-NH_2 corresponds well to those reported previously [47,57], demonstrating the successful synthesis of UiO-66-NH_2 . The XRD peaks of pure $\text{Cd}_{0.2}\text{Zn}_{0.8}\text{S}$ exhibit an obvious left-shift compared to the standard of sphalerite ZnS due to the formation of $\text{Cd}_{0.2}\text{Zn}_{0.8}\text{S}$ solid solution [1,58]. The XRD patterns of $\text{Cd}_{0.2}\text{Zn}_{0.8}\text{S@UiO-66-NH}_2$ composites show no obvious diffraction peak attributable to UiO-66-NH_2 when the UiO-66-NH_2 content is less than 20 wt%, which may be due to the low content of UiO-66-NH_2 . However, the composites with higher UiO-66-NH_2 loading clearly display the diffraction peaks of UiO-66-NH_2 and $\text{Cd}_{0.2}\text{Zn}_{0.8}\text{S}$, reflecting a two-phase composition of UiO-66-NH_2 and $\text{Cd}_{0.2}\text{Zn}_{0.8}\text{S}$ in these composites.

The morphologies and microstructures of the as-prepared samples were characterized by TEM and HRTEM. As shown in Fig. 2a, the pure UiO-66-NH_2 displays a cube morphology, and the size of these cubes is about 50–80 nm. The pristine $\text{Cd}_{0.2}\text{Zn}_{0.8}\text{S}$ sample exhibits uniform particle morphology with the diameter of 10–20 nm (Fig. 2b). The TEM image of CZS@UN20 shows that the $\text{Cd}_{0.2}\text{Zn}_{0.8}\text{S}$ nanoparticles are well dispersed on the surface of the

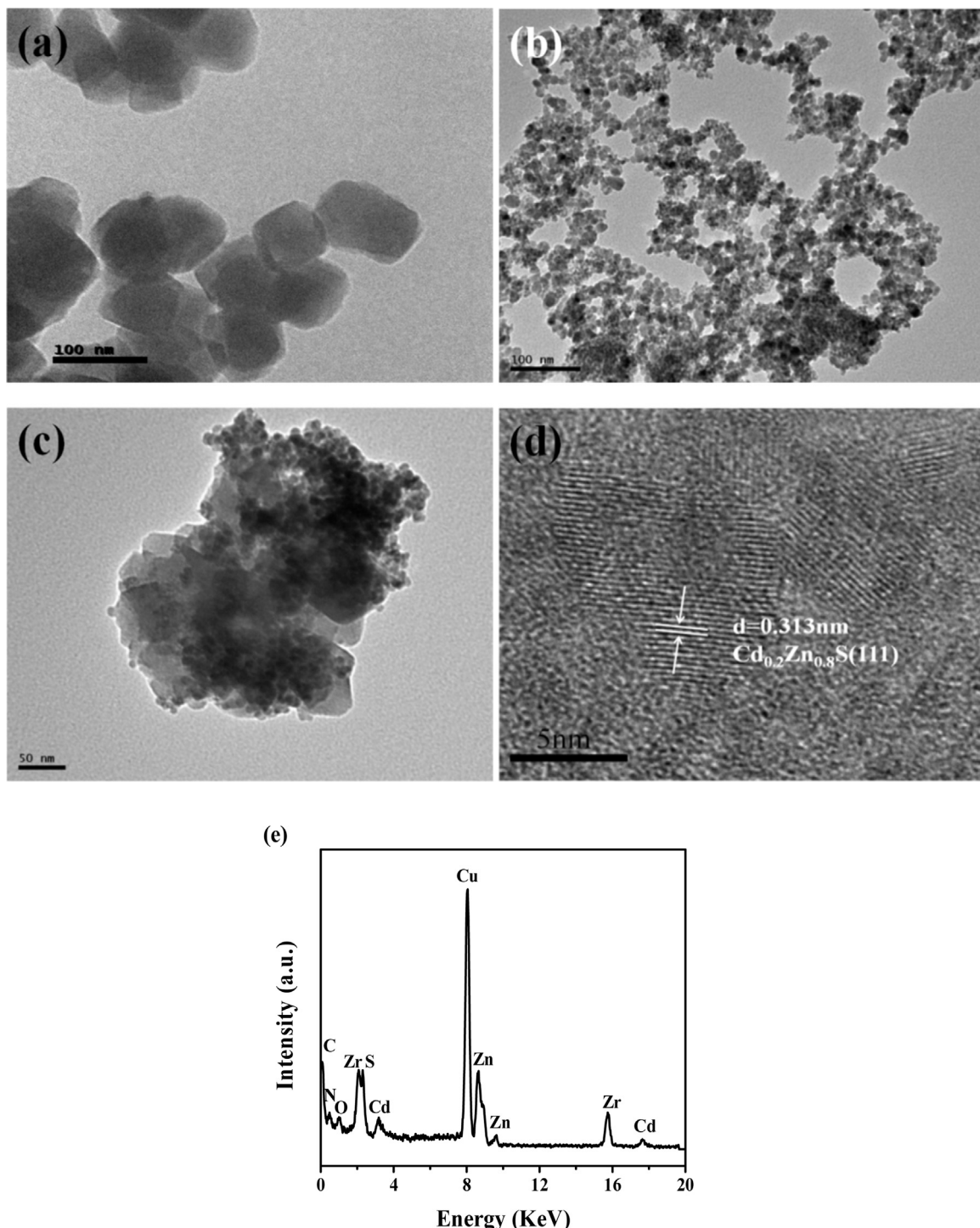


Fig. 2. TEM images of (a) UiO-66-NH₂, (b) Cd_{0.2}Zn_{0.8}S, (c) CZS@UN20, (d) HRTEM image of CZS@UN20, and (e) EDX spectrum of CZS@UN20.

UiO-66-NH₂ cubes (Fig. 2c). The high resolution TEM (HRTEM) image (Fig. 2d) of CZS@UN20 shows clear fringes with lattice spacing of ca. 0.313 nm, which corresponds to the (111) plane of Cd_{0.2}Zn_{0.8}S [1,58]. The EDX spectrum (Fig. 2e) confirms the presence of Cd, Zn, S, Zr, C, O and N elements in the composite.

The composition and chemical state of the Cd_{0.2}Zn_{0.8}S@UiO-66-NH₂ composite were investigated by XPS. The survey spectrum (Fig. 3a) indicates that the sample is composed of C, N, O, Zr, Cd, Zn and S, which is in good agreement with the EDX results. Fig. 3b shows the binding energies of Cd 3d_{5/2} and Cd 3d_{3/2} peaks at

404.7 and 411.5 eV respectively, which are typical values for Cd²⁺ in CdS [15,58,59]. As shown in Fig. 3c, two peaks recorded in the Zn 2p region at 1022.1 and 1045.5 eV are in agreement with the literature data for Zn²⁺ in ZnS [15,58,59]. The S 2p core-level spectrum (Fig. 3d) shows two peaks at 161.3 eV and 162.4 eV, which imply that S is in sulfide state [15,58,59]. The curves of Zr 3d region (Fig. 3e) can be deconvoluted into two peaks for Zr 3d_{5/2} and Zr 3d_{3/2} located at around 182.1 eV and 184.3 eV respectively, which indicates the existence of Zr⁴⁺ [15,58,59]. The C 1s spectrum shown in Fig. 3f can be deconvoluted into three peaks located at

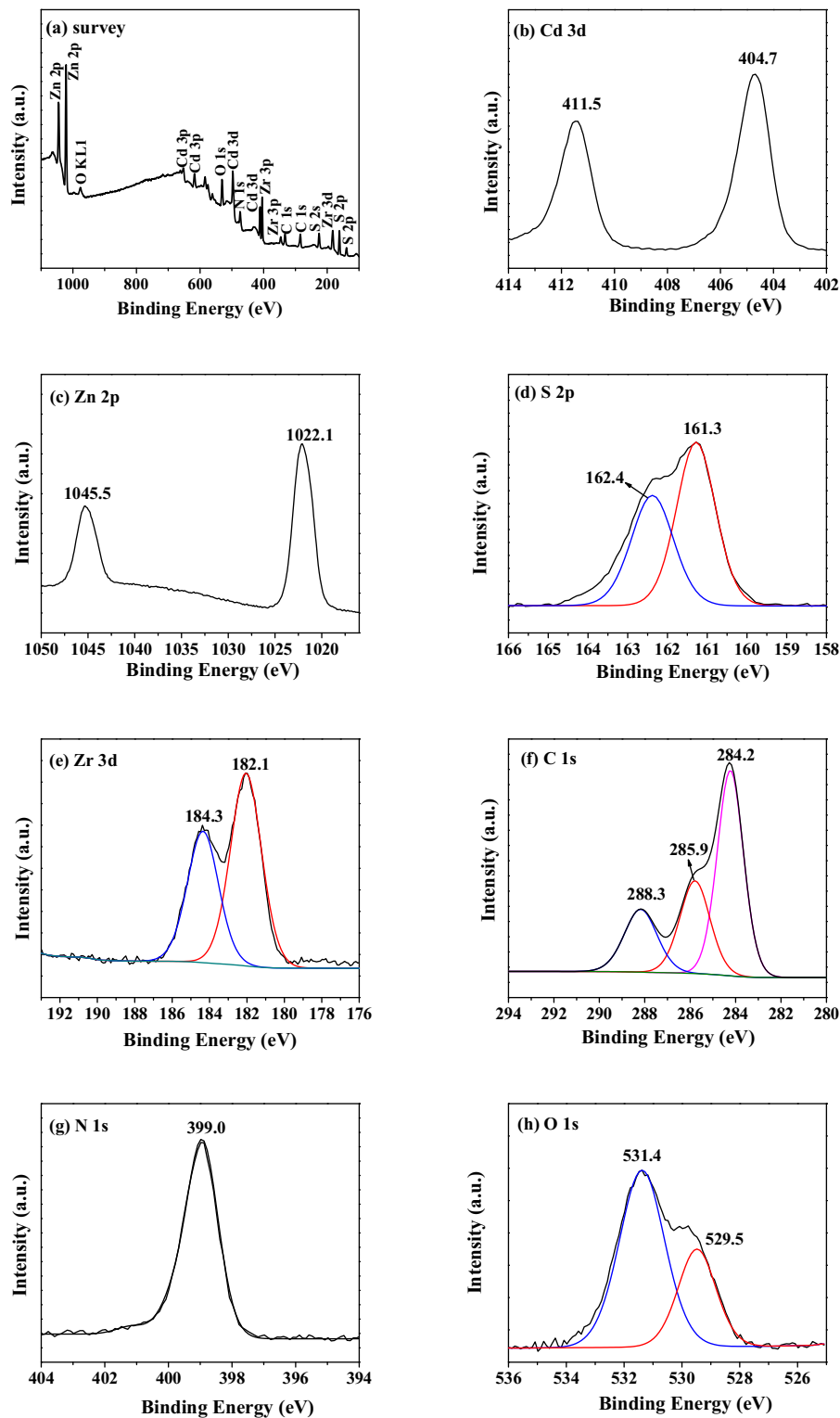


Fig. 3. XPS spectra of CZS@UN20: (a) survey, (b) Cd 3d, (c) Zn 2p, (d) S 2p, (e) Zr 3d, (f) C 1s, (g) N 1s, (h) O 1s.

284.2, 285.9 and 288.3 eV. These three peaks can be assigned to the carbon components on the benzene ring, the C–NH₂ species and the carboxylate (O—C=O) groups of the ATA linkers, respectively [55,60,61]. The N 1s XPS spectrum (Fig. 3g) of Cd_{0.2}Zn_{0.8}S@UiO-66-NH₂ is located at 399.0 eV, which can be attributed to N species in the NH₂ group [55,60,61]. The high-resolution XPS spectrum of the O 1s orbital can be fitted by two peaks at binding energies of around 531.4 and 529.5 eV (Fig. 3h), which are attributed to the

oxygen components on the carboxylate groups of the ATA linkers and the Zr—O bonds of UiO-66-NH₂, respectively [55,60,61].

The N₂ adsorption-desorption measurement was carried out to study the specific surface area and porosity of the as-prepared samples, as shown in Fig. 4 and Table 1. The isotherm of UiO-66-NH₂ belongs to the typical type I, indicating its typical microporous structure [62,63]. The Horvath-Kawazoe (HK) micropore size distribution of UiO-66-NH₂ (Fig. 4b) reveals three major pores at 0.6,

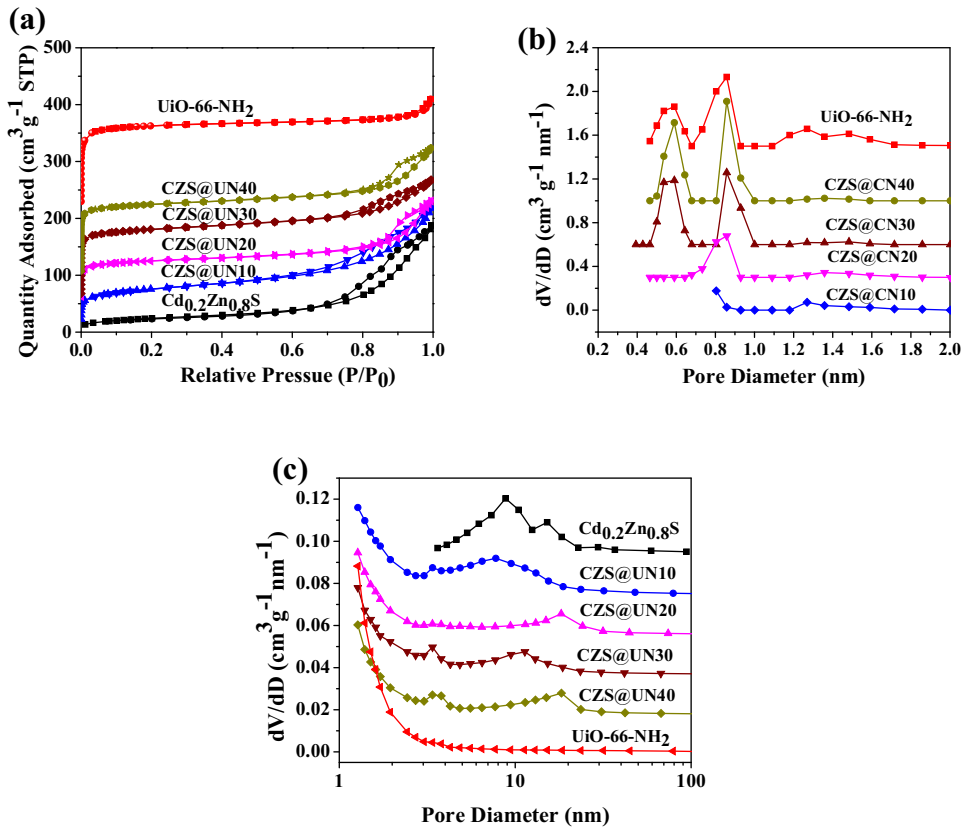


Fig. 4. (a) N₂ adsorption-desorption isotherms, (b) Horvath-Kawazoe (HK) micropore size distributions, and (c) Barrett-Joyner-Halenda (BJH) mesopore size distributions of as-prepared samples.

Table 1

Summary of textural properties and photocatalytic activities of the samples.

Sample	S_{BET} (m ² g ⁻¹)	Pore volume (cm ³ g ⁻¹)	Average Pore Size (nm)	H_2 evolution rate (μmol h ⁻¹ g ⁻¹)	CH ₃ OH production rate (μmol h ⁻¹ g ⁻¹)
Cd _{0.2} Zn _{0.8} S	85.2	0.0559	12.02	2804.2	2.0
CZS@UN10	201.0	0.2551	4.75	4591.6	4.1
CZS@UN20	266.0	0.2741	3.26	5846.5	6.8
CZS@UN30	381.3	0.3882	2.46	5235.9	5.9
CZS@UN40	491.1	0.3982	2.43	4922.7	5.3
UiO-66-NH ₂	967.6	0.5626	1.78	0	0

0.9 and 1.3 nm, which agree quite well with the crystal model and previously-reported values [62,63]. The as-prepared Cd_{0.2}Zn_{0.8}S displays a type IV isotherm with a H3 typical hysteresis loop, indicating the presence of mesoporous structure [64,65]. These mesopores may come from the interstitial voids among Cd_{0.2}Zn_{0.8}S nanoparticles. All Cd_{0.2}Zn_{0.8}S@UiO-66-NH₂ samples exhibit hybrid type I/IV isotherms with large hysteresis between adsorption and desorption branches, revealing the presence of a combination of micropores and mesopores. The existence of both micro- and mesopores can be confirmed by the corresponding pore size distributions as shown in Fig. 4b and c. As shown in Table 1, the BET specific surface areas of pristine UiO-66-NH₂ and Cd_{0.2}Zn_{0.8}S are 967.6 and 85.2 m² g⁻¹, respectively. All Cd_{0.2}Zn_{0.8}S@UiO-66-NH₂ composites have higher specific surface areas than Cd_{0.2}Zn_{0.8}S and the specific surface area of the composites increase with the enhancement of UiO-66-NH₂ contents. Similarly, because of the larger total pore volume of pristine UiO-66-NH₂ than that of pristine Cd_{0.2}Zn_{0.8}S, the total pore volumes of Cd_{0.2}Zn_{0.8}S@UiO-66-NH₂ composites are also increased with the increase of UiO-66-NH₂ content.

The optical absorption of different Cd_{0.2}Zn_{0.8}S@UiO-66-NH₂ composites, pristine UiO-66-NH₂ and Cd_{0.2}Zn_{0.8}S samples were measured by UV-vis. As illustrated in Fig. 5, the pristine UiO-

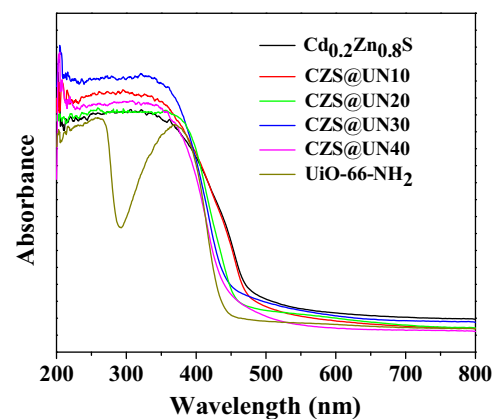


Fig. 5. UV-vis spectra of pure UiO-66-NH₂, Cd_{0.2}Zn_{0.8}S and Cd_{0.2}Zn_{0.8}S@UiO-66-NH₂ composites.

66-NH₂ shows the strong absorption bands in the range of 200–450 nm. The absorption edge value for Cd_{0.2}Zn_{0.8}S is observed at 500 nm. The Cd_{0.2}Zn_{0.8}S@UiO-66-NH₂ composites have absorp-

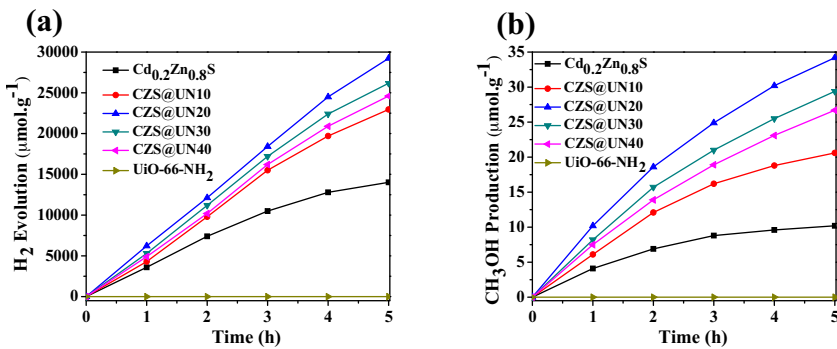


Fig. 6. Plots of (a) photocatalytic H₂ evolution amount and (b) photocatalytic CO₂ reduction amount vs. irradiation time.

tion edges of longer wavelengths in comparison with the pristine UiO-66-NH₂. Similar phenomena were also observed for other MOF-based photocatalysts [53,54]. The slightly red shift might suggest that the composites can absorb more visible light, which may result in generation of more electron-hole pairs. The band gap of Cd_{0.2}Zn_{0.8}S and HOMO-LUMO gap of UiO-66-NH₂ can be calculated by the following equation: $\alpha h\nu = A(h\nu - E_g)^{n/2}$, in which α , $h\nu$, E_g , and A are the absorption coefficient, Planck constant, the light frequency, the band gap (HOMO-LUMO gap), and a constant, respectively. The value of n depends on the type of optical transition of the semiconductor ($n=1$ for direct transition and $n=4$ for indirect transition). For UiO-66-NH₂ and Cd_{0.2}Zn_{0.8}S, the n value of 1 is used [54,58,66]. Therefore, as can be seen from Fig. S4, the corresponding band gap value of Cd_{0.2}Zn_{0.8}S and HOMO-LUMO gap value of UiO-66-NH₂ are estimated to be 2.62 and 2.87 eV, respectively. The band gap energies of Cd_{0.2}Zn_{0.8}S can be calculated by the following equation:

$$E_{VB} = X - E^e + 0.5E_g,$$

where E_{VB} represents valence band (VB) edge potential, X is the electronegativity of the semiconductor estimated by the geometric mean of the electronegativity of the constituent atoms. E^e is the energy of free electrons on the hydrogen scale (~ 4.5 eV), E_g is the band gap energy of the semiconductor. The conduction band (CB) edge potential (E_{CB}) can be determined by $E_{CB} = E_{VB} - E_g$. The X value of pure Cd_{0.2}Zn_{0.8}S is about 5.25 eV. The E_{VB} of bare Cd_{0.2}Zn_{0.8}S can be assigned to be +2.06 eV, and the corresponding E_{CB} of Cd_{0.2}Zn_{0.8}S can be estimated to be -0.56 eV. Some researches reveal that LUMO potential of UiO-66-NH₂ is at -0.60 eV [47,57], thus its HOMO potential is at 2.27 eV.

3.2.2. Photocatalytic activity

The photocatalytic H₂-production over the as-prepared Cd_{0.2}Zn_{0.8}S@UiO-66-NH₂ composites was evaluated under visible light irradiation ($\lambda > 420$ nm) using Na₂S and Na₂SO₃ as sacrificial agents. As shown in Fig. 6a and Table 1, the photocatalytic H₂-production rate is negligible when UiO-66-NH₂ alone is used as photocatalyst, indicating that UiO-66-NH₂ did not act as an effective photocatalyst by itself. Pristine Cd_{0.2}Zn_{0.8}S shows some photocatalytic H₂-production activity, but the rate of H₂ evolution is low ($2804.2 \mu\text{mol h}^{-1} \text{g}^{-1}$). After the introduction of UiO-66-NH₂, the H₂-production performance of Cd_{0.2}Zn_{0.8}S is significantly enhanced. The photoactivity of the Cd_{0.2}Zn_{0.8}S@UiO-66-NH₂ composites is found to be dependent on the content of UiO-66-NH₂. With the increased content of UiO-66-NH₂ from 10 wt% to 20 wt%, the photocatalytic H₂ evolution rate of the hybrid catalyst increases from 4591.6 to 5846.5 $\mu\text{mol h}^{-1} \text{g}^{-1}$. A further increase in the content of UiO-66-NH₂ leads to a reduction in the photocatalytic activity. This decrease is probably due to the following

factors: (i) accompanying with the increase of UiO-66-NH₂, the content of the Cd_{0.2}Zn_{0.8}S, which is the only activity phase, will be decreased relatively. (ii) overmuch UiO-66-NH₂ may turn into a recombination center of photoinduced charges (this can be confirmed by the photoluminescence measurement as shown in Fig. 8a), which will cause reduction of activity. The maximum photocatalytic H₂ generation rate ($5846.5 \mu\text{mol h}^{-1} \text{g}^{-1}$) is obtained when the UiO-66-NH₂ content is 20 wt%, which is about 2.1 times higher than that of pure Cd_{0.2}Zn_{0.8}S.

The photocatalytic activities of the Cd_{0.2}Zn_{0.8}S@UiO-66-NH₂ composites were also evaluated by using them for the photoreduction of CO₂ dissolved in NaOH solutions under visible-light irradiation. Control experiments indicate that no appreciable reduction products were detected in the absence of either photocatalyst or light irradiation, indicating that all the products obtained during the reaction were produced by the photocatalysts. The photocatalytic activity results for all the samples toward the conversion of CO₂ with H₂O are shown in Fig. 6b and Table 1. Only methanol is detected as a product using Cd_{0.2}Zn_{0.8}S or the Cd_{0.2}Zn_{0.8}S@UiO-66-NH₂ composites as photocatalysts, which is in line with the previous published work that CH₃OH is the main reduction product in aqueous CO₂ photoreduction systems [67–69]. It can be observed that pristine UiO-66-NH₂ is not active for photocatalytic CO₂ reduction. The bare Cd_{0.2}Zn_{0.8}S without UiO-66-NH₂ shows a low photocatalytic activity for CO₂ reduction, in which the CH₃OH production rate is only $2.0 \mu\text{mol h}^{-1} \text{g}^{-1}$. All the Cd_{0.2}Zn_{0.8}S@UiO-66-NH₂ samples exhibit a superior photocatalytic activity for reduction of CO₂ compared with the bare Cd_{0.2}Zn_{0.8}S. The UiO-66-NH₂ content has a significant influence on the photocatalytic activity of Cd_{0.2}Zn_{0.8}S. Among the as-prepared samples, CZS@UN20 presents the highest CH₃OH evolution amount ($6.8 \mu\text{mol h}^{-1} \text{g}^{-1}$) during visible-light irradiation, which is about 3.4 times higher than that of pure Cd_{0.2}Zn_{0.8}S.

The catalyst lifetime is of great importance besides the photocatalytic performance. The CZS@UN20 hybrid was used as the representative sample to examine the long-term stability of the Cd_{0.2}Zn_{0.8}S@UiO-66-NH₂ composites for photocatalytic H₂ production and CO₂ reduction. As shown in Fig. 7a and b, after four recycles, both the H₂ evolution rate and the activity of photocatalytic CO₂ reduction did not show a significant decrease. The structure of the CZS@UN20 sample before and after four consecutive cycles was also recorded by XRD. As shown in Fig. S5, no apparent change in the crystalline structure is observed before and after the reaction. Moreover, the ICP results (Table S2) demonstrate that the leaching of the cadmium and zinc ions is so small that it can be ignored. Based on the above results, it clearly suggests that the as-prepared Cd_{0.2}Zn_{0.8}S@UiO-66-NH₂ composites have relatively high stabilities during photocatalytic H₂ production and reduction of CO₂.

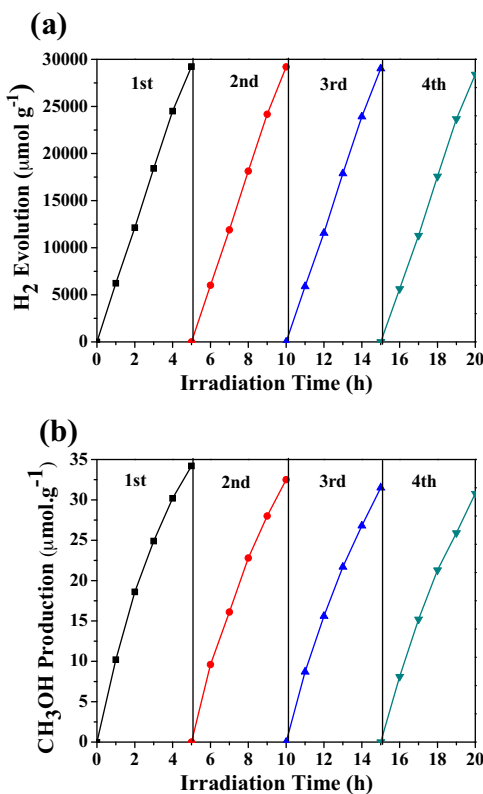


Fig. 7. Cycle runs of (a) photocatalytic H₂ production and (b) CO₂ reduction over the CZS@UN20 photocatalyst.

3.2.3. Enhanced visible-light photocatalytic activity mechanism

In order to understand the enhanced photocatalytic mechanism of the Cd_{0.2}Zn_{0.8}S@UiO-66-NH₂ composites, PL spectroscopy measurements to analyze the charge recombination of semiconductor were investigated. Fig. 8a presents the PL spectra of pure Cd_{0.2}Zn_{0.8}S, CZS@UN10, CZS@UN20, CZS@UN30 and CZS@UN40 samples at room temperature with an excitation wavelength of 360 nm. As observed from Fig. 8a, the pure Cd_{0.2}Zn_{0.8}S exhibits a strong emission peak at around 475 nm. When the UiO-66-NH₂ was added, the PL emission intensity decreases markedly, which suggests that the photoinduced charge could be efficiently separated when the heterojunction was formed between UiO-66-NH₂ and Cd_{0.2}Zn_{0.8}S. The order of PL intensity is Cd_{0.2}Zn_{0.8}S > CZS@UN10 > CZS@UN40 > CZS@UN30 > CZS@UN20, which agrees well with the observed results of their photocatalytic activity mentioned above.

The improved carrier separation efficiency of the Cd_{0.2}Zn_{0.8}S@UiO-66-NH₂ composites was further confirmed by the transient photocurrent responses of UiO-66-NH₂, Cd_{0.2}Zn_{0.8}S and CZS@UN20. As shown in Fig. 8b, the pure UiO-66-NH₂ sample shows a very low photocurrent density, which can be attributed to the fast recombination of photogenerated electrons and holes in UiO-66-NH₂. The pure Cd_{0.2}Zn_{0.8}S has photocurrent under visible light irradiation, corresponding to the photo excitation of the semiconductor. The Cd_{0.2}Zn_{0.8}S@UiO-66-NH₂ composite shows the highest photocurrent density, indicating the efficient photo-generated charge transfer between Cd_{0.2}Zn_{0.8}S and UiO-66-NH₂. The PL and photocurrent results confirmed the superior charge transfer and recombination inhibition in the Cd_{0.2}Zn_{0.8}S@UiO-66-NH₂ composite photocatalyst, which is responsible for the enhanced photocatalytic activity.

On the basis of the above results, a possible interface electron transfer behavior and the corresponding photocatalytic mechanisms for H₂ production and CO₂ reduction are demonstrated and illustrated in Scheme 1. Under visible-light irradiation, UiO-66-NH₂ and Cd_{0.2}Zn_{0.8}S were excited to generate electron-hole pairs. Since the LUMO potential of UiO-66-NH₂ (−0.60 eV vs. NHE) is more negative than the CB potential of Cd_{0.2}Zn_{0.8}S (−0.56 eV vs. NHE), the photoinduced electrons on the LUMO of UiO-66-NH₂ can directly transfer to the CB of Cd_{0.2}Zn_{0.8}S, which could inhibit the recombination of photoinduced electron-hole pairs and prolong the lifetime of photoinduced charge carriers. In the photocatalytic H₂ production, the electrons at the CB of Cd_{0.2}Zn_{0.8}S can reduce the adsorbed H⁺ to evolve H₂. The holes at the VB (HOMO) were consumed by the sacrificial reagents (Na₂S and Na₂SO₃). In the case of the photocatalytic CO₂ reduction, the active valence band (HOMO) holes can oxidize H₂O to produce •OH, which can release O₂ and H⁺ [70]. Then, H⁺ and the CB electrons would reduce CO₂ to CH₃OH [70].

4. Conclusions

In summary, highly active Cd_{0.2}Zn_{0.8}S@UiO-66-NH₂ composite photocatalysts have been successfully synthesized by a facile solvothermal process. The resultant hybrids exhibited significantly enhanced photocatalytic activity for hydrogen evolution and CO₂ reduction under visible light irradiation as compared with pristine components. The optimum loading content of UiO-66-NH₂ is determined to be ~20 wt% and the corresponding H₂ evolution rate and CH₃OH production rate are 5846.5 μmol h⁻¹ g⁻¹ and 6.8 μmol h⁻¹ g⁻¹, respectively. The remarkable enhancement of photocatalytic activity can be ascribed to the efficient charge separation and transfer on the interface between Cd_{0.2}Zn_{0.8}S and UiO-66-NH₂. Moreover, the Cd_{0.2}Zn_{0.8}S@UiO-66-NH₂ photocatalysts exhibited good recyclability under visible-light irradiation. The Cd_{0.2}Zn_{0.8}S@UiO-66-NH₂ hybrids introduced in this work, with high photocatalytic activity and excellent photostability, are a very

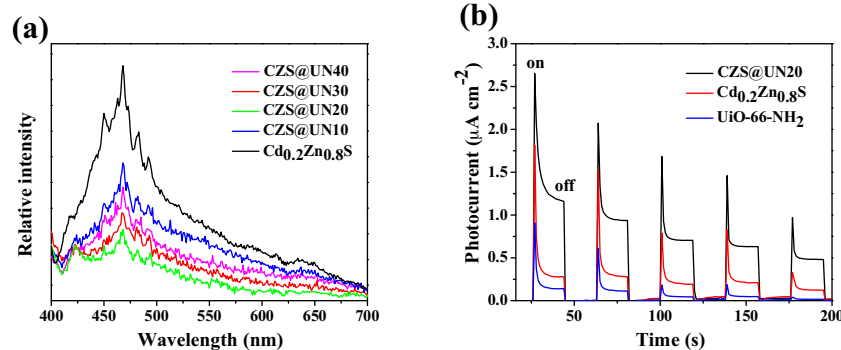
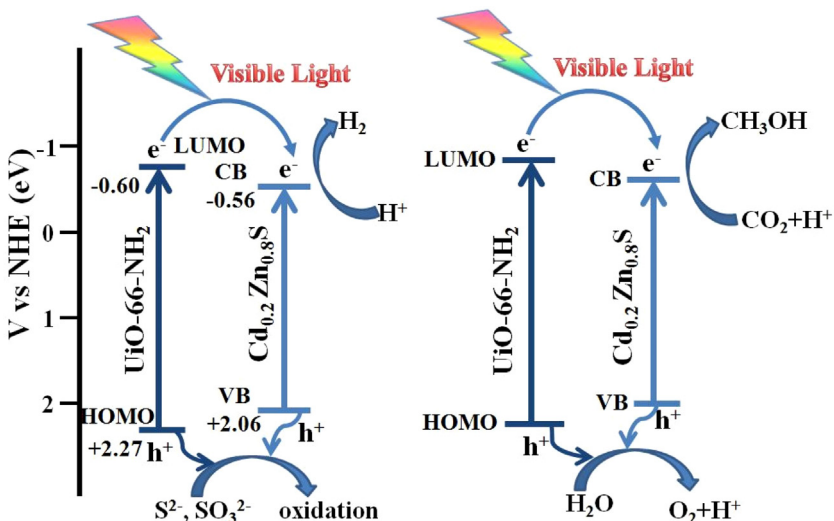


Fig. 8. (a) PL spectra and (b) photocurrent spectra of the as-synthesized samples.



Scheme 1. Schematic diagram of the photogenerated electrons and holes transfer in the $\text{Cd}_{0.2}\text{Zn}_{0.8}\text{S}@\text{UiO-66-NH}_2$ composite and the mechanism of photocatalytic H_2 production and CO_2 reduction under visible light irradiation.

promising candidate for possible practical application in high-performance H_2 production and CO_2 reduction.

Acknowledgments

The authors gratefully acknowledge the follow-up Program for Professor of Special Appointment in Shanghai (Eastern Scholar), the National Natural Science Foundation of China (11472164, 51271105), Shanghai Science & Technology Committee (15520720600) and Innovative Research Team (IRT13078) for financial support. The authors also thank Lab for Microstructure, Instrumental Analysis & Research Center, Shanghai University for materials characterizations.

Appendix A. Supplementary data

Supplementary data associated with this article can be found, in the online version, at <http://dx.doi.org/10.1016/j.apcatb.2016.07.032>.

References

- [1] J. Zhang, J.G. Yu, M. Jaroniec, J.R. Gong, *Nano Lett.* 12 (2012) 4584–4589.
- [2] M.Q. Yang, N. Zhang, M. Pagliaro, Y.J. Xu, *Chem. Soc. Rev.* 43 (2014) 8240–8254.
- [3] X.J. Lang, X.D. Chen, J.C. Zhao, *Chem. Soc. Rev.* 43 (2014) 473–486.
- [4] H. Tong, S.X. Ouyang, Y.P. Bi, N. Umezawa, M. Oshikiri, J.H. Ye, *Adv. Mater.* 24 (2012) 229–251.
- [5] J.L. White, M.F. Baruch, J.E. Pander, Y. Hu, I.C. Fortmeyer, J.E. Park, T. Zhang, K. Liao, J. Gu, Y. Yan, T.W. Shaw, E. Abelev, A.B. Bocarsly, *Chem. Rev.* 115 (2015) 12888–12935.
- [6] B. Seger, T. Pedersen, A.B. Laursen, P.C.K. Vesborg, O. Hansen, I. Chorkendorff, *J. Am. Chem. Soc.* 135 (2013) 1057–1064.
- [7] C. Yin, S.M. Zhu, Z.X. Chen, W. Zhang, J.J. Gua, D. Zhang, *J. Mater. Chem. A* 1 (2013) 8367–8378.
- [8] L.W. Zhang, C. Baumanis, L. Robben, T. Kandiel, D. Bahnemann, *Small* 19 (2011) 2714–2720.
- [9] S.C. Yan, J.J. Wang, Z.G. Zou, *Dalton Trans.* 42 (2013) 12975–12979.
- [10] Q. Liu, D. Wu, Y. Zhou, H.B. Su, R. Wang, C.F. Zhang, S.C. Yan, M. Xiao, Z.G. Zou, *ACS Appl. Mater. Interfaces* 6 (2014) 2356–2361.
- [11] Q.L. Gu, K.J. Zhu, N.S. Zhang, Q.M. Sun, P.C. Liu, J.S. Liu, J. Wang, Z.S. Li, *J. Phys. Chem. C* 119 (2015) 25956–25964.
- [12] C.L. Li, J. Yuan, B.Y. Han, W.F. Shangguan, *Int. J. Hydrogen Energy* 36 (2011) 4271–4279.
- [13] L. Wang, W.Z. Wang, M. Shang, W.Z. Yin, S.M. Sun, L. Zhang, *Int. J. Hydrogen Energy* 35 (2010) 19–25.
- [14] S.N. Garaje, S.K. Apte, S.D. Naik, J.D. Ambekar, R.S. Sonawane, M.V. Kulkarni, A. Vinu, B.B. Kale, *Environ. Sci. Technol.* 47 (2013) 6664–6672.
- [15] D.H. Wang, L. Wang, A.W. Xu, *Nanoscale* 4 (2012) 2046–2053.
- [16] Z.H. Han, G. Chen, C.M. Li, Y.G. Yu, Y.S. Zhou, *J. Mater. Chem. A* 3 (2015) 1696–1702.
- [17] Y.X. Li, D. Gao, S.Q. Peng, G.X. Lu, S.B. Li, *Int. J. Hydrogen Energy* 36 (2011) 4291–4297.
- [18] M.N. Huang, J.H. Yu, C.S. Deng, Y.H. Huang, M.G. Fan, B. Li, Z.F. Tong, F.Y. Zhang, L.H. Dong, *Appl. Surf. Sci.* 365 (2016) 227–239.
- [19] W.J. Li, D.Z. Li, S.G. Meng, W. Chen, X.Z. Fu, Y. Shao, *Environ. Sci. Technol.* 45 (2011) 2987–2993.
- [20] I. Hod, W. Bury, D.M. Karlin, P. Deria, C.W. Kung, M.J. Katz, M. So, B. Klahr, D. Jin, Y.W. Chung, T.W. Odom, O.K. Farha, J.T. Hupp, *Adv. Mater.* 26 (2014) 6295–6300.
- [21] J.W. Liu, L.F. Chen, H. Cui, J.Y. Zhang, L. Zhang, C.Y. Su, *Chem. Soc. Rev.* 43 (2014) 6011–6061.
- [22] W. Cai, C.C. Chu, G. Liu, Y.J. Wang, *Small* 37 (2015) 4806–4822.
- [23] D. Alezi, Y. Belmabkhout, M. Suyetin, P.M. Bhatt, L.J. Weselinski, V. Solovyeva, K. Adil, I. Spanopoulos, P.N. Trikalitis, A.H. Emwas, M. Eddaoudi, *J. Am. Chem. Soc.* 137 (2015) 13308–13318.
- [24] Z.X. Zhao, X.L. Ma, A. Kasik, Z. Li, Y.S. Lin, *Ind. Eng. Chem. Res.* 52 (2013) 1102–1108.
- [25] A. Herbst, A. Khutia, C. Janiak, *Inorg. Chem.* 53 (2014) 7319–7333.
- [26] Y.P. He, Y.X. Tan, J. Zhang, *Inorg. Chem.* 52 (2013) 12758–12762.
- [27] J.D. Rocca, D.M. Liu, W.B. Lin, *Acc. Chem. Res.* 44 (2011) 957–968.
- [28] M.G. Campbell, D. Sheberla, S.F. Liu, T.M. Swager, M. Dinca, *Angew. Chem.* 127 (2015) 4423–4426.
- [29] C. Adhikari, A. Das, A. Chakraborty, *Mol. Pharm.* 12 (2015) 3158–3166.
- [30] F.X.L. Xamena, A. Corma, H. Garcia, *J. Phys. Chem. C* 111 (2007) 80–85.
- [31] M.C. Das, H. Xu, Z.Y. Wang, G. Srinivas, W. Zhou, Y.F. Yue, V.N. Nesterov, G.D. Qian, B.L. Chen, *Chem. Commun.* 47 (2011) 11715–11717.
- [32] Y.P. Yuan, L.S. Yin, S.W. Cao, G.S. Xu, C.H. Li, C. Xue, *Appl. Catal. B: Environ.* 168–169 (2015) 572–576.
- [33] C. Wang, Z.G. Xie, K.E. Krafft, W.B. Lin, *J. Am. Chem. Soc.* 133 (2011) 13445–13454.
- [34] D.R. Sun, Y.H. Gao, J.L. Fu, X.C. Zeng, Z.N. Chen, Z.H. Li, *Chem. Commun.* 51 (2015) 2645–2648.
- [35] C.F. Zhang, L.G. Qiu, F. Ke, Y.J. Zhu, Y.P. Yuan, G.S. Xu, X. Jiang, *J. Mater. Chem. A* 1 (2013) 14329–14334.
- [36] D.K. Wang, M.T. Wang, Z.H. Li, *ACS Catal.* 5 (2015) 6852–6857.
- [37] K.G.M. Laurier, F. Verwoortele, R. Ameloot, D.E.D. Vos, J. Hofkens, M.B.J. Roeffaers, *J. Am. Chem. Soc.* 135 (2013) 14488–14491.
- [38] R.W. Liang, F.F. Jing, L.J. Shen, N. Qin, L. Wu, J. Hazard. Mater. 287 (2015) 364–372.
- [39] D.K. Wang, R.K. Huang, W.J. Liu, D.R. Sun, Z.H. Li, *ACS Catal.* 4 (2014) 4254–4260.
- [40] W.T. Xu, L. Ma, F. Ke, F.M. Peng, G.S. Xu, Y.H. Shen, J.F. Zhu, L.G. Qiu, Y.P. Yuan, *Dalton Trans.* 43 (2014) 3792–3798.
- [41] D.R. Sun, L. Ye, Z.H. Li, *Appl. Catal. B: Environ.* 164 (2015) 428–432.
- [42] Y.H. Fu, D.R. Sun, Y.J. Chen, R.K. Huang, Z.X. Ding, X.Z. Fu, Z.H. Li, *Angew. Chem. Int. Ed.* 51 (2012) 3364–3367.
- [43] H.P. Jing, C.C. Wang, Y.W. Zhang, P. Wang, R. Li, *RSC Adv.* 4 (2014) 54454–54462.
- [44] D.R. Sun, Y.H. Fu, W.J. Liu, L. Ye, D.K. Wang, L. Yang, X.Z. Fu, Z.H. Li, *Chem. Eur. J.* 19 (2013) 14279–14285.
- [45] D.K. Wang, Z.H. Li, *Catal. Sci. Technol.* 5 (2015) 1623–1628.
- [46] L.J. Shen, M.B. Luo, Y.H. Liu, R.W. Liang, F.F. Jing, L. Wu, *Appl. Catal. B: Environ.* 166–167 (2015) 445–453.

[47] L.J. Shen, S.J. Liang, W.M. Wu, R.W. Liang, L. Wu, *J. Mater. Chem. A* 1 (2013) 11473–11482.

[48] D.R. Sun, W.J. Liu, M. Qiu, Y.F. Zhang, Z.H. Li, *2015, Chem. Commun.* 51 (2015) 2056–2059.

[49] D.R. Sun, W.J. Liu, Y.H. Fu, Z.X. Fang, F.X. Sun, X.Z. Fu, Y.F. Zhang, Z.H. Li, *Chem. Eur. J.* 20 (2014) 4780–4788.

[50] W.W. Zhan, Q. Kuang, J.Z. Zhou, X.J. Kong, Z.X. Xie, L.S. Zheng, *J. Am. Chem. Soc.* 135 (2013) 1926–1933.

[51] R. Li, J.H. Hu, M.S. Deng, H.L. Wang, X.J. Wang, Y.L. Hu, H.L. Jiang, J. Jiang, Q. Zhang, Y. Xie, Y.J. Xiong, *Adv. Mater.* 26 (2014) 4783–4788.

[52] Y.L. Xu, M.M. Lv, H.B. Yang, Q. Chen, X.T. Liu, F.Y. Wei, *RSC Adv.* 5 (2015) 43473–43479.

[53] Z. Sha, J.L. Sun, H.S.O. Chan, S. Jaenicke, J.S. Wu, *RSC Adv.* 4 (2014) 64977–64984.

[54] Z. Sha, J.S. Wu, *RSC Adv.* 5 (2015) 39592–39600.

[55] R. Wang, L.N. Gu, J.J. Zhou, X.L. Liu, F. Teng, C.H. Li, Y.H. Shen, Y.P. Yuan, *Adv. Mater. Interfaces* 2 (2015) 1500037.

[56] C. Gomes Silva, I. Luz, F.X. Llabres i Xamena, A. Corma, H. Garcia, *Chem. Eur. J.* 16 (2010) 11133–11138.

[57] L.J. Shen, S.J. Liang, W.M. Wu, R.W. Liang, L. Wu, *Dalton Trans.* 42 (2013) 13649–13657.

[58] H. Liu, Z.T. Jin, Z.Z. Xu, *Dalton Trans.* 44 (2015) 14368–14375.

[59] L.J. Zhang, T.F. Jiang, S. Li, Y.C. Lu, L.L. Wang, X.Q. Zhang, D.J. Wang, T.F. Xie, *Dalton Trans.* 42 (2013) 12998–13003.

[60] L.J. Shen, W.M. Wu, R.W. Liang, R. Lin, L. Wu, *Nanoscale* 5 (2013) 9374–9382.

[61] W. Zhu, P.J. Liu, S.N. Xiao, W.C. Wang, D.Q. Zhang, H.X. Li, *Appl. Catal. B: Environ.* 172–173 (2015) 46–51.

[62] Z.G. Hu, Y.W. Peng, Z.X. Kang, Y.H. Qian, D. Zhao, *Inorg. Chem.* 54 (2015) 4862–4868.

[63] Y.T. Han, M. Liu, K.Y. Li, Y. Zuo, Y.X. Wei, S.T. Xu, G.L. Zhang, C.S. Song, Z.C. Zhang, X.W. Guo, *CrystEngComm* 17 (2015) 6434–6440.

[64] H. Liu, Y. Su, P. Chen, Y. Wang, *J. Mol. Catal. A: Chem.* 378 (2013) 285–292.

[65] L. Shi, L. Liang, J. Ma, F.X. Wang, J.M. Sun, *Dalton Trans.* 43 (2014) 7236–7244.

[66] S.F. Li, X. Wang, Q. Chen, Q.Q. He, M.M. Lv, X.T. Liu, J.P. Lv, F.Y. Wei, *RSC Adv.* 5 (2015) 53198–53206.

[67] J.Y. Wang, G.B. Ji, Y.S. Liu, M.A. Gondal, X.F. Chang, *Catal. Commun.* 46 (2014) 17–21.

[68] T. Ohno, T. Higo, N. Murakami, H. Saito, Q.T. Zhang, Y. Yang, T. Tsubota, *Appl. Catal. B: Environ.* 152–153 (2014) 309–316.

[69] J. Mao, T.Y. Peng, X.H. Zhang, K. Li, L.Q. Ye, L. Zan, *Catal. Sci. Technol.* 3 (2013) 1253–1260.

[70] R. Gusain, P. Kumar, O.P. Sharma, S.L. Jain, O.P. Khatri, *Appl. Catal. B: Environ.* 181 (2016) 352–362.